A&A 441, 1043–1054 (2005)
DOI: 10.1051/0004-6361:20053344

Astronomy & Astrophysics

The Galactic plane region near $\ell = 93°$

III. Multi-wavelength emission from SNR 3C 434.1

T. Foster[1,2]

[1] National Research Council of Canada, Herzberg Institute of Astrophysics, Dominion Radio Astrophysical Observatory, PO Box 248, Penticton, BC V2A 6J9, Canada
e-mail: Tyler.Foster@nrc-cnrc.gc.ca
[2] Dept. of Physics, University of Alberta, Edmonton, Alberta, T6G 2J1, Canada

Received 30 April 2005 / Accepted 27 June 2005

ABSTRACT

New Canadian Galactic Plane Survey radio continuum, ROSAT X-ray, and optical line observations of supernova remnant (SNR) 3C 434.1 (G94.0+1.0) are presented. A radio spectrum of index $\alpha = 0.4$ (where $S \propto \nu^{-\alpha}$) confirms this SNR's emission signature as predominantly synchrotron, and suggests the SNR is in the Sedov expansion phase. The morphology of the remnant is compared in X-ray, optical, and radio continuum, and the brightest emission in all three wavelength regimes is from the eastern hemisphere of 3C 434.1, which marks where the SNR shock is interacting with the inside wall of its stellar wind bubble (SWB) home. The system is determined to be 4.5 kpc distant, residing in the Perseus Arm Spiral shock. From a deep Hα mosaic of the region, λ656 nm Hα line emission is observed that correlates well with radio synchrotron emission and anticorrelates with X-ray emission from the SNR. The origin of this optical emission is likely dense ($n_e = 40$ cm^{-3}) cooling H II from the wall of the SWB, where the SNR shock has penetrated and become radiative ($v_s \sim 100$ km s^{-1}). The X-ray spectrum of this SNR between 0.5 and 2.4 keV is well modelled by a single-temperature thermal plasma ($T_e = 4.5 \times 10^6$ K, $n_e = 0.2$ cm^{-3}). The magnetic field of the bright radio synchrotron emission region is found (under the assumption of near equipartition) to be $B \sim 15$ μG, a factor of 3 compression of the ambient ISM field (5 μG). The westward extension of 3C 434.1 is the result of ongoing free expansion of the shock into the lower density interior of the SWB. I use multiwavelength observations to arrive at a unique solution for an interaction model of 3C 434.1 with the SWB, from which the age ($t = 25\,000$ yr) and mass ejected in the explosion ($M_{ej} = 15.5\ M_\odot$) are determined. I also find an initial blast-wave velocity of 1350 km s^{-1}, typical of type 1b SNe.

Key words. ISM: supernova remnants – ISM: bubbles

1. Introduction

I continue the survey of the Galactic plane region near $\ell = 93°$ presented in Paper I (Foster & Routledge 2001) and Paper II (Foster Routledge & Kothes 2004) with a multi-wavelength study of the emission from SNR 3C 434.1 ($\ell = 94°$, $b = +1°$). The 21 cm continuum appearance of this object is similar to the nearby H II region NRAO 655, discussed in Paper I. The space between these two objects appears filled by dim continuum emission, and the objects appear bridged by this nebulosity. We have explained the eastward extension of NRAO 655 as the result of this region's "champagne" outflow through the inside edge of its host molecular cloud. The overall appearance suggests a connection between 3C 434.1 and this H II region, as the faint extended emission from both seem to point towards each other. We continued our investigation of this group in Paper II and here present a thorough look at 3C 434.1 and its surroundings.

Goss et al. (1984) present the 608.5 MHz and 4.75 GHz continuum morphology of 3C 434.1 as indicative of a shell-type remnant, with a spectral index ($\alpha = 0.44$) confirming a synchrotron origin for its radio emission. These authors also detect polarized 4.75 GHz emission (mean total 6%) from the remnant. They conclude with speculation that the SNR and nearby objects NRAO 655, NRAO 652, and others (see Fig. 1 in Paper I) may be at a common distance. Further observations are called for by Goss et al. to clarify this. A more recent 1420 MHz study of 3C 434.1 comes from Landecker et al. (1985), whose conclusions concerning the SNR do not differ significantly from previous authors. No further observations of 3C 434.1 and its surroundings have been published since then.

In Paper II, we have presented the discovery of a shell of atomic hydrogen that surrounds the remnant, from which a radial velocity for 3C 434.1 is found. The extragalactic source 4C 51.45 on the SNR's northern limb allows an H I absorption spectrum to be measured, and provides a unique means of determining the dynamics of this stellar wind bubble, which

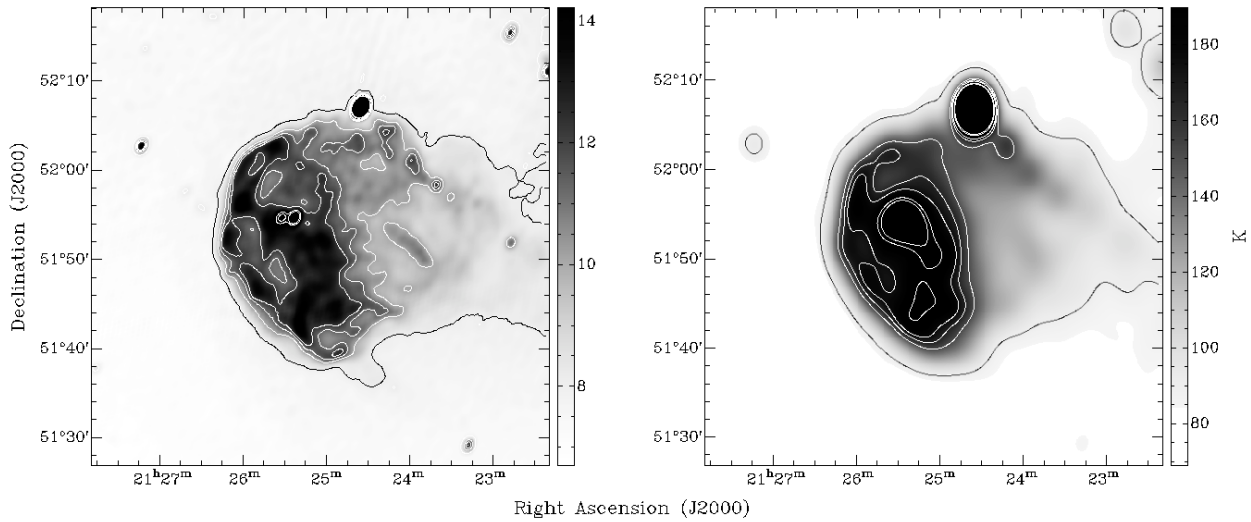

Fig. 1. Radio continuum appearance of the SNR 3C 434.1 in CGPS data, at 1420 MHz (*left panel*) and 408 MHz (*right panel*). 1420 MHz contour levels are at 8 (black contour), 10, 11.2, 12.1, 16, and 18 K. 408 MHz contour levels are 90 (black contour), 150, 165, 176, 200, and 210 K.

is modelled as an homologously expanding ellipsoidal shell. Centred within this shell and shown to be related are one O4 type star and three B0 type stars. The energy of the SWB demands another (deceased) O4 star, likely the predecessor to 3C 434.1, the remnant of a core-collapse event of type 1b or 1c.

The lack of any reliable distance measurement for 3C 434.1 has prevented an in-depth look at its physical structure and conditions. On the basis of a new distance from the aforementioned method of Foster (2005), and new observations in radio, X-ray and optical wavelengths, I offer a fresh look at this SNR.

2. Observations and data reduction

2.1. Radio

The CGPS field of 3C 434.1 was observed at 1420 MHz and 408 MHz with the Synthesis Telescope at the Dominion Radio Astrophysical Observatory (DRAO). I present the 21 cm and 74 cm continuum images of the region in Fig. 1. The continuum observations are centred on $(\ell, b) = (93.466°, 1.000°)$ and are part of the Canadian Galactic Plane Survey (CGPS), a project by a consortium of researchers from five countries to map a large segment of the northern Galactic plane in radio and infrared wavelengths at a resolution approaching 1′ (Taylor et al. 2003). The FWHM of the beams achieved in the survey are $49'' \times 49''\mathrm{cosec}\,\delta$ and $2.8' \times 2.8'\mathrm{cosec}\,\delta$ resolution at 1420 MHz and 408 MHz, respectively. The continuum data at 21 cm have an intrinsic uncertainty due to calibration of ±5%, and are ±10% uncertain at 74 cm. Other relevant parameters of the telescope and data reduction procedures are given in Sect. 2.1 in Paper I, and further detail on the DRAO Synthesis Telescope can be found in Landecker et al. (2000).

To depict accurately the sky in the radio continuum and H I line images (especially those of large angular size), missing short-spacing information is added to each ST map. These data were obtained from the Effelsberg 21 cm Galactic Plane Survey (Reich et al. 1990), and the 408 MHz All-Sky Survey (Haslam et al. 1982).

115 GHz carbon monoxide spectral line ^{12}CO($J = 1$–0) data towards the $\ell = 93°$ region were obtained from the Columbia CO survey of Dame et al. (2001; data provided courtesy of Dame). Each channel is separated by 1.3 km s^{-1}; spatial resolution is 8.5′.

2.2. X-ray

3C 434.1 was observed on 1992 November 15 using the X-ray telescope on ROSAT with the Position Sensitive Proportional Counter (PSPC) (Principal Investigator E. Pfeffermann). No other data on this remnant exist in the archives of X-ray missions. The total accepted integration time was 9137 s and the pointing position centres on 3C 434.1: α, δ(J2000) = $21^{\rm h}24^{\rm m}50.4^{\rm s}$, 51°52′48″ ($\ell = 93.973°$, $b = 1.022°$), placing the remnant within the least vignetted and most sensitive part of the telescope field.The energy band of the PSPC has a range of 0.1 keV to 2.4 keV divided into 240 bins, with the soft band covering 0.1–0.4 keV, and the hard band 0.4–2.4 keV. Data were reduced with the PROS software package in IRAF, and smoothed hard- and soft-band images, corrected for vignetting, are created. Very little soft-band flux (below 0.5 keV) is seen from 3C 434.1, likely the result of a large column density in this line of sight.

2.3. Optical

Observations towards 3C 434.1 in the [O III] (λ502 nm), Hα+[N II] (λ656 nm) and [S II] (λ672 nm) emission lines were made at the University of Alberta's Devon Astronomical Observatory (DevonAO). Detailed information on the DevonAO system and these observations are found in Paper I, and Foster et al. (1999). The SNR field centre is $(\alpha, \delta) = (21^{\rm h}25^{\rm m}4^{\rm s}, 51°52'52'')$ in J2000 coordinates. Further,

Table 1. Summary of observations centred on and surrounding SNR 3C 434.1, carried out at the Devon AO.

Observation date	Field center (α, δ)(J2000)	Total $I_{\rm time}$(s)	Filter
Nov. 04 1999	$21^{\rm h}25^{\rm m}4^{\rm s}$, 51°52′52″	9600	Hα+[N II]
Dec. 04, Dec. 07 1999	$21^{\rm h}25^{\rm m}4^{\rm s}$, 51°52′52″	16800	[O III]
Dec. 23, Dec. 24 1999	$21^{\rm h}25^{\rm m}4^{\rm s}$, 51°52′52″	13200	[S II]
Jan. 27 2001	$21^{\rm h}22^{\rm m}2^{\rm s}$, 51°44′19″	7200	Hα+[N II]
Jan. 24 2001	$21^{\rm h}23^{\rm m}11^{\rm s}$, 52°8′20″	6000	Hα+[N II]
Jan. 26 2001	$21^{\rm h}27^{\rm m}8^{\rm s}$, 51°34′45″	8400	Hα+[N II]
Jan. 23 2001	$21^{\rm h}27^{\rm m}11^{\rm s}$, 52°9′29″	7200	Hα+[N II]

I have observed four additional fields surrounding 3C 434.1 in the Hα+[N II] band and a mosaic of the region was created. 19 h of total integration was spent on the SNR and surrounding fields over several nights (see Table 1). Multiple 600 s integrations of each $27' \times 27'$ field are averaged into a composite final frame, and these final frames assembled into a mosaic using IRAF software.

To maximize the S/N ratio of faint nebulosity while preserving its photometric value, I have developed a simple method to create a single composite photometrically accurate CCD frame from many individuals. This technique is necessary since each frame is taken at slightly different altitude (and hence airmass). After basic CCD image processing (including removal of cosmic rays and bad pixels), a uniform background (in analog-digital units, or ADU) for each target frame is determined from areas outside the SNR's radio continuum boundary. This level is subtracted from individual frames. As the transparency of each night varies, first-order extinction coefficients k'_λ (in units of ADU per unit airmass) for each filter wavelength are determined nightly from photometry of bright field stars, and/or photometric observations of planetary nebulae. The frames are then scaled to a common airmass of 0 by multiplying them by the factor:

$$f = 10^{\frac{k'_\lambda X_{\rm observed}}{2.5}} \quad (1)$$

where $X_{\rm observed}$ is the airmass at which the frame was made. In this way, the flux of each is corrected to extra-atmospheric values without affecting the background. Each frame is shifted to a common centre, and a mean image (corrected for atmospheric extinction) is added to the mosaic. A PSF is fitted to each frame and stars are removed, using the DAOPHOT package (Stetson 1987) included in the IRAF distribution.

To calibrate the data for photometry, the Hα+[N II] flux (in ADU) from the remaining nebulosity is converted to erg cm^{-2} s^{-1} sr^{-1} with a gain calibration factor determined from DevonAO observations of bright planetary nebulae (NGCs 6543, 6210 and 7027) with the same filter. Published line fluxes for these nebulae are from Keyes et al. (1990), Manchado & Pottasch (1989) and Acker et al. (1989). Expected fluxes from the N II lines (λ = 654.8 nm and λ = 658.3 nm) are accounted for, calculated using typical intrinsic (unreddened) intensity ratios of observed for SNRs (e.g. Fesen & Hurford 1995, 1996; Fesen et al. 1997). Expected N II fluxes are 15% (λ = 658.3 nm) and 8% (λ = 654.8 nm) of the Hα flux.

The starless Hα mosaic of 3C 434.1 and surroundings is finally convolved to 1′ resolution to match that of the 21 cm radio continuum resolution, and to improve the signal-to-noise level of extended nebulous emission. Figure 4 shows the final mosaic, which has an uncertainty in the photometric calibration of 24%. No significant flux is observed in the [O III] band, and barely significant emission correlating with the Hα+[N II] is observed in the [S II] band.

3. Continuum appearance and radio spectrum of 3C 434.1

Figure 1 shows the 1420 and 408 MHz continuum images of 3C 434.1. The angular resolution of the two images is $1' \times 1.2'$ and $3.4' \times 4.3'$, respectively. The shell of 3C 434.1 follows a very circular boundary in the East, with this symmetry disrupted in the western half by emission that appears to be "spilling" westward (see black contour in Fig. 1). The remnant displays classical shell structure, with a circle of diameter $26' \pm 1.5'$ best fitting the radio continuum boundary in the east. The remnant appears divided into East-West halves, with the eastern half a mean 2.5–3 K (21 cm continuum temperature) brighter than the fainter western half. The appearance is of a spherical balloon being ripped open on the West side and gas spilling in this direction. The 21 cm brightness temperature of the continuum emission falls linearly toward the West at a rate of 0.1 K arcmin^{-1}, and indicates very little exponential or power-law behaviour. If the area west of the SNR is an essentially evacuated region into which gas is expanding into, a linear density profile is expected only after a significant period of time. In a spectral index map of four frequencies (see Sect. 3.1), significant non-thermal emission from the SNR is observed out to at least 30 pc West of the centre (see Sect. 4), but beyond this the emission is too feeble to conclude that it is associated with the SNR. Nonetheless, the process of the SNR's expansion to the West must be advanced, negating a very young age for 3C 434.1.

The CGPS data also includes polarization at 21 cm, however, no polarized structure to 3C 434.1 at all is observed. This is likely due to the remnant's substantial distance of 4.5 kpc, towards which a critical amount of foreground ISM mass would depolarize its emission. In discussing the structure of Hα emission observed towards this remnant (Sect. 5) I will refer to a 21 cm continuum feature (shown in Fig. 1) similar to a semi-circular "hook" of emission. This feature is visible on the south-east face of the remnant (α, δ = $21^{\rm h}25^{\rm m}$, 51°40′). As well, a "bar" of radio emission is attached to this hook, extending north-east to the shell's eastern edge.

Table 2. The integrated flux density and intensity of 3C 434.1 at eight radio frequencies. References for the data measured by us are: (2) Vessey et al. (1998); (3) Rengelink et al. (1996); (4) CGPS, this work; and (5) Fürst et al. (1990). References for published flux densities are (6) Goss et al. (1984). Intensities I_ν are calculated from S_ν/Ω, where Ω is the angular area of the radio SNR.

ν (MHz)	Ref.	Resolution (arcmin)	$S_{3C\,434.1}$ (Jy)	I_ν (10^{-18} erg cm^{-2} s^{-1} Hz^{-1} sr^{-1})
151	2	1.2×1.5	26.5 ± 2.1	3.3 ± 0.3
325	3	0.9×1.1	17.6 ± 3.5	2.8 ± 0.6
408	4	3.4×4.3	16.9 ± 2.1	2.5 ± 0.2
608.5	6	1.7	16 ± 1.7	2.3 ± 0.3
1420	4	1.06×61.2	12.86 ± 60.7	1.86 ± 60.2
2695	5	4.3	7.8 ± 0.8	1.2 ± 0.1
4750	6	2.4	7.2 ± 0.5	1.1 ± 0.1

3.1. Radio spectrum

Radio continuum data at 5 frequencies (151, 325, 408, 1420 and 2695 MHz) is obtained, and the integrated flux density of 3C 434.1 at each frequency is calculated. Flux densities and uncertainties for 3C 434.1 are measured with polygonal aperture photometry tasks under IRAF. Errors in measurements reflect both photometric uncertainty (the variation in flux from nine separate aperture measurements), and errors intrinsic to the data due to uncertainties in calibration. These are (from the references listed in Table 2): ±5% and ±10% for 1420 and 408 MHz CGPS data respectively, ±4–10% for the 151 MHz survey, ∼10% for 2695 MHz survey, and 15–25% for the 325 MHz WENSS data (for which the flux is not entirely trustworthy due to missing short-baseline interferometer data). The bright point source on the north edge (4C 51.45) was excluded from flux density measurements, as it is most likely extragalactic (its continuum emission is absorbed by the entire H I column – Paper II).

I also obtain flux densities for 3C 434.1 at 608.5 MHz and 4.75 GHz from the literature (also referenced in Table 2). The remnant's radio spectrum traced by all seven frequencies in the table follows a power law of $S_\nu(\mathrm{Jy}) \propto \nu^{-\alpha}$, with an index of $\alpha = 0.38 \pm 0.03$ (Fig. 2). This value is slightly lower than that of Mantovani et al. (1982, $\alpha = 0.46 \pm 0.03$) and consistent with Goss et al. (1984, $\alpha = 0.44 \pm 0.04$). Our value is moderately lower than expected for typical shell-type remnants ($\alpha = 0.45$–0.55), suggesting that parts of the SNR are perhaps in a more advanced stage of expansion.

A spectral index (SI) map of 3C 434.1 is calculated with radio continuum 151 MHz, 408 MHz, 1420 MHz and 2695 MHz maps. The map shows very little variation (<10%) in the spectrum's slope ($\alpha = 0.38$) across the eastern face of the remnant. The westerly extension of 3C 434.1 appears to have a slightly flatter spectrum ($\alpha \leq 0.3$) than the radio shell. Along with the overall smoothness of the SI map, the spectrum of 3C 434.1 is linear over the observed range of frequencies, and exhibits no breaks. This is interpreted as evidence that differences in the particle acceleration across the visible extent of the SNR shock are negligible. The SI of 3C 434.1 is much flatter than early phase SNRs (typically $\alpha = 0.6$ to 0.8), and reflects an advanced adiabatic expansion stage.

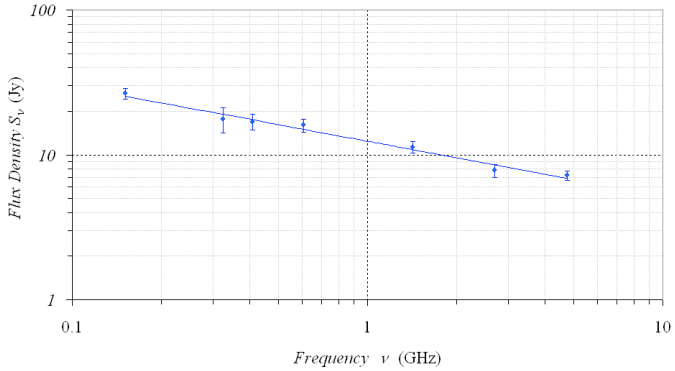

Fig. 2. The radio spectrum of 3C 434.1, calculated with CGPS data (1420 and 408 MHz flux values), and additional radio data (see Table 2). The best-fitted line shown has gradient of $\alpha = 0.38 \pm 0.03$, a spectral index characteristic of a shell type remnant.

4. The distance to 3C 434.1

CTB104A (G93.7−0.3) and 3C 434.1 are the only known supernova remnants in this vicinity of the Galactic plane, with SNR DA530 (G93.3+6.9) displaced a large angular distance from the plane. The large radial velocity of 3C 434.1 ($v_{\mathrm{LOS}} = -78$ km s^{-1}) and a circular rotation law suggests it is very distant at 9 kpc (using a flat rotation curve with solar constants of $R_0 = 8.5$ kpc and $v_0 = 220$ km s^{-1}), a value that almost certainly can be dismissed as inaccurate by the unreasonably large diameter indicated for the remnant (80 pc).

One of the foundations of this study of 3C 434.1 is a new non-kinematic distance. Using the distance method of Foster & Routledge (2003), a distance of $d = 5.2 \pm 1.1$ kpc to the SNR/SWB system was reported in Paper II. This distance method gauges an object's distance from a turbulence-smoothed velocity field, derived by registering the column density-velocity relation $N_{\mathrm{HI}}(v)$ in H I data with the column density-distance relation $N_{\mathrm{HI}}(r)$ from the H I spatial model (e.g. open circles in Fig. 3). Recent development of this distance method (Foster 2005) include a revised density model for the H I disk, and a circular velocity field for the gas, perturbed by model density wave and shock motions. The model velocity field that is fit to the observations is used for estimating distances from an object's velocity. We fit the model of Foster (2005) to H I spectral line data in the direction $\ell = 94°$, $b = +1°$ (Fig. 3, top), and obtain the fitted velocity field (Fig. 3, bottom). The systemic velocity of the SWB/SNR system ($v_{\mathrm{LOS}} \sim -78$ km s^{-1}, Paper II) shows that the SNR could reside in the ridge of the Perseus arm spiral shock, the model for which is 4.5 kpc distant in this direction. The multiply-valued velocity-distance relation near the shock suggests the SNR could also be 6.5 kpc distant, placing the system beyond the shock and on the far edge of the Perseus arm (the arm is 4.7 kpc distant in the fitted density model).

A simple line of reasoning will show that 6.5 kpc is probably not the true distance. Supposing that it is, then for $\ell = 94°$ the galactocentric distance is $R = 10.3$ kpc. Assuming circular rotation (angular velocity $\Omega = 220/10.3 = 21.3$ km s^{-1} kpc^{-1}) and a pitch angle for the arm of 12° (assumed a logarithmic spiral travelling at pattern speed $\Omega_{\mathrm{p}} = 10$ km s^{-1} kpc^{-1}), the

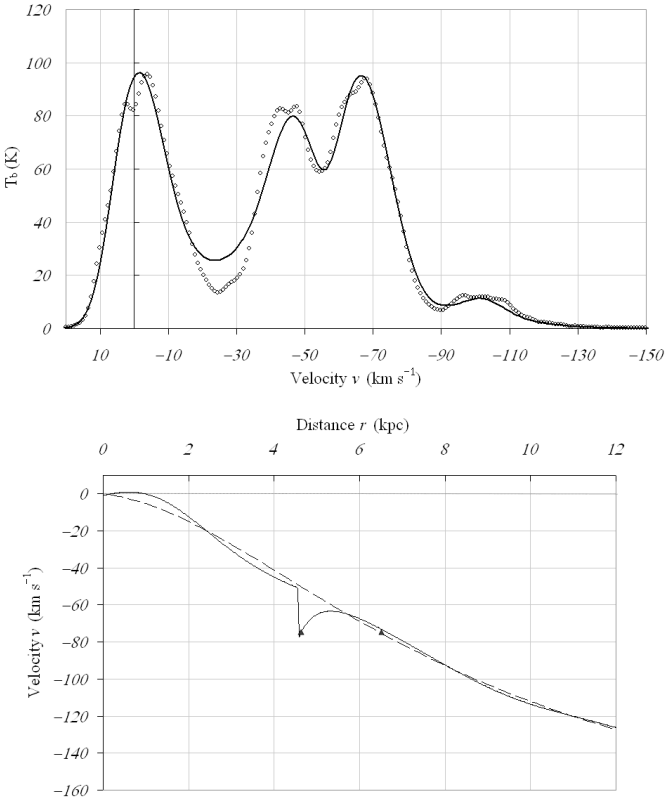

Fig. 3. (*Top*) The observed H I profile towards $\ell = 94°$, $b = +1°$, and the fitted model from the H I modelling method of Foster (2005). (*Bottom*) The model velocity field that fits the H I density model to the observed spectra at top is shown as the solid curve. Triangles mark the possible distances to the SNR, which is either in the Perseus arm spiral shock (4.5 kpc) or just beyond the arm (6.5 kpc). The circular velocity field unperturbed by streaming or shock motions is shown as a dashed line.

system would have entered the shock some 66 Myr ago and since migrated through the arm to a position 6.5 kpc distant from the Sun. If the stars in the SWB (including the SNR's progenitor) formed from the compression of the shock, then their age (maximum 2.6 Myr, Paper II) is quite inconsistent with this time. The distance of 4.5 kpc places the SNR within the shock, which *is* consistent with the O4 type star found residing in the SWB (Paper II), whose expected lifetime is only 2.6 Myr.

The uncertainty in the distance to 3C 434.1 will arise from the uncertainty in our fitted model parameters, and the uncertainty in $v_{\rm LOS}$ due to turbulent dispersion σ_v (the LOS-averaged value for which is 5.8 km s^{-1}, from the fitted model). The formal uncertainty in the model fit (determined in Foster 2005) imparts ±0.8 kpc uncertainty to the distance, and the turbulence another ±0.5 kpc. The final determination for 3C 434.1 is $d = 4.5 \pm 0.9$ kpc. A physical size of 1.3 pc corresponds to 1 arcminute on the sky, and a physical diameter of $D = 34$ pc is calculated for 3C 434.1.

4.1. The column density from radio line emission

We can also use the value of the X-ray absorbing column density (found below in Sect. 6) and 1′-resolution CGPS H I and 9′-resolution ^{12}CO data (from the Columbia CO survey of Dame et al. 2001) to resolve the distance ambiguity to the SNR. The following relation finds the total line-of-sight column density $N_{\rm H}$ of hydrogen nuclei:

$$\begin{aligned} N({\rm H})({\rm cm}^{-2}) &= N({\rm H\,I}) + 2N({\rm H_2}) \\ &= 1.82\times10^{18}\int \frac{T_{\rm s}}{({\rm K})}\tau(v)\frac{{\rm d}v}{({\rm km\,s^{-1}})} \\ &\quad +2X_{\rm CO}\int \frac{T_{\rm b}({\rm CO})}{({\rm K})}\frac{{\rm d}v}{({\rm km\,s^{-1}})} \end{aligned} \quad (2)$$

where $T_{\rm s}$ is the spin temperature of the H I, and $X_{\rm CO}$ is the ratio between $N({\rm H_2})$ (units of cm^{-2}) and the integrated CO temperature (units of K km s^{-1}). This equation accounts for ISM components that are expected to contribute the most to the absorbing column (warm and cool H I, and molecular H_2 gas). The value of Eq. (2) integrated to 3C 434.1 should be comparable to the absorbing column from the X-ray model only if integrated velocity channels contain only gas that is spatially in front of the remnant. This assertion will fail if the SNR is within the shock, as the shock introduces velocity reversals (whereby H I around the shock is closer to us than gas at the same velocity that follows normal circular rotation). If the SNR is at the *greater* distance of 6.5 kpc (see Fig. 3), the integrated column should be equal to or less than the X-ray value ($N_{\rm H} = 1.58\times10^{22}$ cm^{-2}).

The bright extragalactic source 4C 51.45 is situated on the SNR's northern limb, and its continuum absorption offers a probe of the warm and cool neutral hydrogen column towards 3C 434.1. This absorbing column is calculated with CGPS H I data, and the On-Off method outlined by Strasser & Taylor (2004). Integrated to ∼–78 km s^{-1} (the systemic velocity of the SWB) the total H I column to 3C 434.1 is $N({\rm H\,I}) \simeq 1.6\times10^{22}$ cm^{-2}. The H_2 column is proportional to the velocity-integrated ^{12}CO brightness by $X_{\rm CO}$. We refer to Young & Scoville (1991) for $X_{\rm CO} \simeq 3\times10^{20}$ cm^{-2} K^{-1} km^{-1} s, a "typical" value for molecular clouds in the disk. Integrating the Columbia CO data towards the SNR gives a molecular hydrogen column to 3C 434.1 of $N({\rm H_2}) \simeq 2\times10^{21}$ cm^{-2}. The total absorbing column to 3C 434.1 is therefore $\sim2\times10^{22}$ cm^{-2}, significantly *higher* than the X-ray absorbing column of $\sim1.58\times10^{22}$ cm^{-2}. However, integrating to the velocity of the shock front (−48 km s^{-1} in the model, Fig. 3) the total column of hydrogen nuclei is 1.3×10^{22} cm^{-2}, *lower* than the X-ray value. This is direct evidence that 3C 434.1 is not at the far distance indicated by circular rotation (6.5 kpc in our model), but rather resides in the nearer shocked zone of the Perseus spiral arm.

4.2. The absence of CO and IR emission from 3C 434.1

At no significant level in the velocity range of the SWB (-69 km s$^{-1} \geq v \geq -93$ km s^{-1}) is any ^{12}CO emission found spatially coincident with 3C 434.1. This apparent lack of CO emission near this remnant may simply be a natural result of the remnant's location within an evacuated stellar wind bubble, but may belie the presence of small angular scale CO cloudlets that are undetected in the low sensitivity 9′ resolution CO data.

The lack of any detectable CO would tend to rule out interaction of the shock with internal molecular condensations. Higher sensitivity and resolution ^{12}CO observations are clearly called for to determine this.

No infrared emission is seen from this SNR in either MSX (8 μm) or IRAS (12, 25, 60 +100 μm) data, indicating an absence of collisionally heated dust. The IR background surrounding the SNR is remarkably smooth, and any structure comparable in scale to the radio SNR would be resolved by these data, so there is no confusion present. The general absence of IR emission suggests either that 3C 434.1 is indeed evolving in a region that contains little dust, or that the evolution of the remnant is extremely advanced, and the shock wave has already cooled to the point where losses due to IR radiation from dust are no longer significant. The former scenario seems the more likely one.

5. Optical emission from 3C 434.1

In a 1.5°×1.5° starless mosiac image at similar resolution to 21 cm radio continuum, faint emission at λ656.3 nm is observed coincident with steep-spectrum radio emission of 3C 434.1 (see Fig. 4). Some of this is undoubtedly superposed foreground (for example, emission from H II region G93.6+1.3, 3 kpc distant), and the entanglement of nebulosity is somewhat confusing. However, within the boundary of the radio continuum remnant is Hα emission that is very distinctly shaped, closely matching the contours of the radio continuum "hook", and following the bright south-eastern rim of continuum emission. As well, Hα emission runs upward (NE) following the "bar" of synchrotron radio emission. There also exists a very apparent anticorrelation between X-ray and this Hα emission that is distinct enough to be unlikely to occur by chance (see Fig. 6). These positive comparisons are evidence that the shock front is indeed located at the position of this optical emission.

These striking correlations/anticorrelations are evidence that the Hα outlined in Fig. 4 is associated with SNR 3C 434.1. The best explanation for the origin of the Hα emission in this SNR is from the interaction of the blast wave with the front inner wall of the surrounding SWB. Therefore, it is probable that the LOS dimension of this ionized hydrogen is roughly comparable to the thickness of the eastern radio shell. From the 21 cm radio continuum image the eastern shell is estimated to be 2′ thick, a thickness-to-radius ratio of $\Delta R/R \sim 0.15$. This is in good agreement with estimates for other shell-type remnants (e.g. KES 79; Seward & Velusamy 1995). From this I estimate the thickness of the H II is ~3 ± 1 pc.

In the following, I treat this emission as originating at 4.5 ± 0.5 kpc and suffering 8.8 ± 0.6 mag of optical extinction (see Sect. 6). The observed flux is $F_{\mathrm{H}\alpha} = 4.5 \pm 1.0{\times}10^{-12}$ erg cm^{-2} s^{-1}, or a surface brightness of $I_{\mathrm{H}\alpha} = 3.3 \pm 0.7$ Rayleighs (1 Rayleigh = $10^6/4\pi$ photons cm^{-2} s^{-1} sr^{-1}). Table 3 lists other observed and calculated physical parameters for the optical emission from 3C 434.1. The emission measure EM is calculated from:

$$EM = 2.75\,(T_{\mathrm{e}})^{0.9}\, I_{\mathrm{H}\alpha} \exp\left[2.2E(B-V)\right] \mathrm{cm}^{-6}\mathrm{pc} \qquad (3)$$

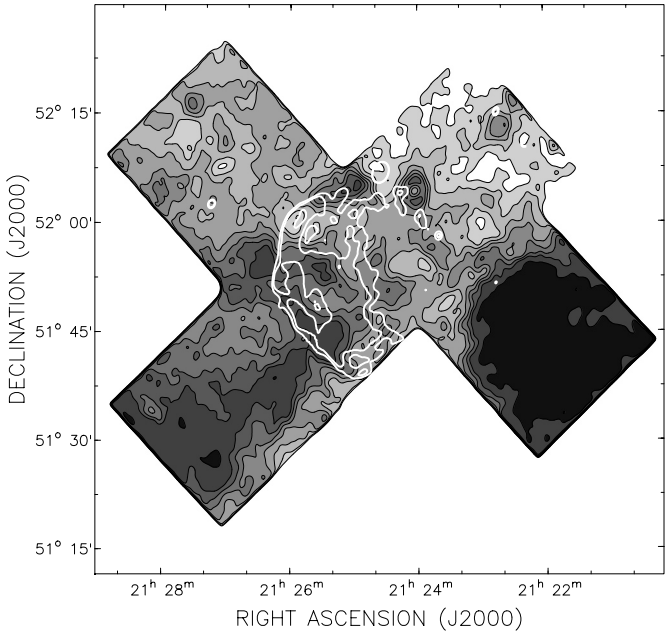

Fig. 4. The Hα CCD composite mosaic towards SNR 3C 434.1 (bright emission is dark in the figure). Some artefacts remain in the image (rings of scattered light around the very brightest stars). White contours shown are the eastern-hemisphere of 21 cm radio emission. The optical emission correlates with the hook-like and bar-like radio features in the SE corner of the SNR. The bright H II region G93.6+1.6 (uncatalogued) is at right.

where T_{e} is in units of 10^4 K, and $I_{\mathrm{H}\alpha}$ in Rayleighs. With $A_{\mathrm{V}}/E(B-V) = 3.1$, one finds $E(B-V) = \simeq 2.8 \pm 0.2$ mag. Assuming $T_{\mathrm{e}} = 10^4$ K, the emission measure is $EM = 4724 \pm 2251$ cm^{-6} pc. The rms mean electron density, $n_{\mathrm{e}} = 40^{+13}_{-11}$ cm^{-3}, is obtained from this measure and the estimated path length through the ionized gas. A mass of ionized hydrogen of 400 $M_\odot$ is also found. Accounting for 35% by mass of He, the thermal energy content of this H II is $E_{\mathrm{th}} = 3/2M/\overline{m}kT_{\mathrm{e}} \sim 1.6{\times}10^{48}$ erg (where $\overline{m} = 0.62$ is the mean atomic mass for a fully ionized plasma of number abundance [He]/[H] = 0.1), a small fraction of the SNR explosion energy.

The absence of emission from [O III] is probably due to either the age of this interaction zone far exceeding the characteristic cooling time of O^{++}, and/or the substantially increased extinction that would be suffered by radiation of λ500 nm.

6. X-ray emission from 3C 434.1

Currently, the only high-energy observations of SNR 3C 434.1 exist in the public archive of the ROSAT mission. ROSAT PSPC-B data for G94.0+1.0 were obtained, and analyzed using the PROS software package under IRAF. Smoothed hard band 0.5 keV $< kT_{\mathrm{e}} <$ 2.4 keV images of the remnant were made and compared to the CGPS radio continuum images.

A circle of radius 13′ (similar to the radio shell) contains the remnant's emission at high energies. As seen in Fig. 5, the SNR's radio continuum and hardband X-ray morphology correlate very well, with the bright hard X-ray emission mostly confined to the eastern radio shell. East-west surface brightness

Table 3. Properties of the Hα line emission seen towards 3C 434.1. The emission measure is related to the electron density via $EM = \int n_e^2 ds$. The thermal energy estimated accounts for 35% by mass of He.

Parameter	Estimated value
Observed:	
Flux $F_{H\alpha}$ (10^{-12} erg cm^{-2} s^{-1})	4.5 ± 1.0
Distance d (kpc)	4.5 ± 0.5
Area of emission (pc^2)	130
Assumed:	
Temperature T_e (K)	10^4
Depth of emission ds (pc)	~3 ± 1
Reddening $E(B-V)$ (mag)	2.8 ± 0.2
Derived:	
Emission measure EM (cm^{-6} pc)	4724 ± 2251
RMS electron density n_e (cm^{-3})	40^{+13}_{-11}
Luminosity $L_{H\alpha}$ (10^{36} erg s^{-1})	6.1 ± 0.4
Mass of ionized hydrogen ($M_\odot$)	400 ± 163
Thermal energy (10^{48} erg)	2.2

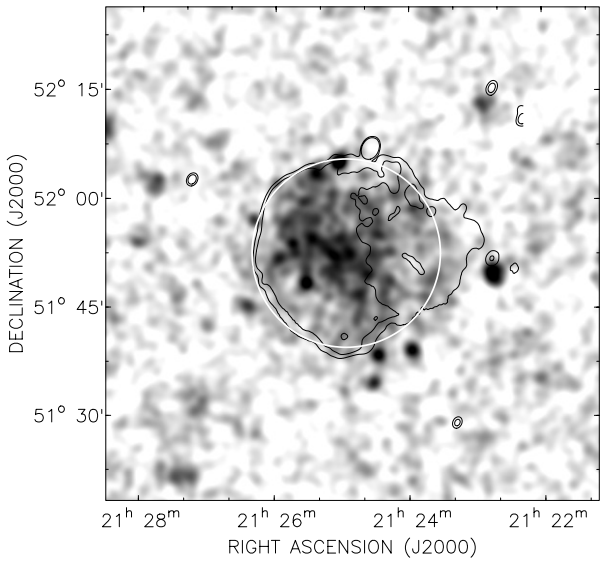

Fig. 5. The hardband X-ray emission of 3C 434.1, as observed by ROSAT in the energy range 0.5–2.4 keV. The 21 cm radio contours are shown, and the 13′ radius aperture from which the X-ray spectrum was extracted is drawn (white circle).

profiles of emission show strongly peaked hard X-rays in the centre of the Eastern radio shell, and the hard X-ray emission falls to background counts at the location of the radio shell's limb in the East. Lower surface brightness X-ray emission in the West correlates with lower brightness radio emission in this region, and the X-rays taper to background counts at a similar rate as radio emission. The remnant appears not to be interacting with very much material in this hemisphere, and is probably still freely-expanding west into the very low density interior of its SWB home (see Fig. 8 of Paper II).

In Fig. 6 one observes a very distinct anticorrelation between the Hα emission identified with 3C 434.1 (see Sect. 5), and hard X-ray emission. The anticorrelation suggests that the Hα and X-ray emission originate from different locations and gaseous components of the remnant. In a "cloudy" medium

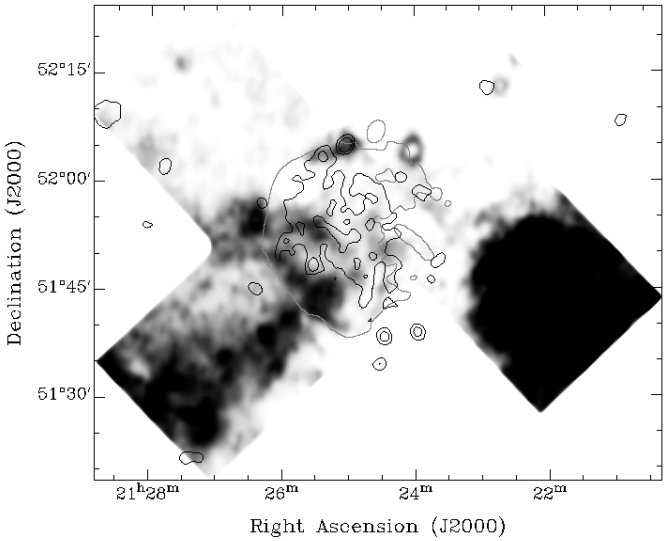

Fig. 6. The Hα mosaic with hardband X-ray contours overlaid (black contours), showing the distinction anti-correlation between bright X-ray emission and optical emission. The SNR's outer radio boundary at 21 cm is drawn as well (gray contour).

(one with sharp density contrasts) such as this one, this is understandable. The Hα originates with dense portions of the SWB wall that are cooling after having been heated by the shock wave, while X-ray emission marks the location of tenuous hot post-shock gas ($T_e > 10^6$ K) from less-dense parts of the inner wall of the SWB recently heated by the shock.

Nominal soft (0.1–0.5 keV) X-ray emission is seen scattered across the face of the SNR. However, there is a conspicuous absence of soft X-ray emission within the eastern radio-bright shell. Scattered patches of such emission are seen inside and outside the radio continuum boundary of 3C 434.1, but no clear correlation is observed. Very little flux in this band is observed for this remnant, suggesting a large absorbing column and distance.

Finally, there is no observed correlation between any radio and X-ray point sources in this field.

A high-energy-band spectrum in 23 channels (from 0.5 keV to 2.4 keV) was extracted from a circle (radius 13′, see Fig. 5) centred on and containing the brightest X-ray emission, and a background was determined from an annulus well outside X-ray flux associated with the SNR (inner radius 17.8′, width 5′, background counts corrected for vignetting of the telescope field). Six point sources within these regions were excluded. The observed spectrum peaks near 1.3 keV. Various models of plasma emission absorbed by a Galactic foreground were fitted to this spectrum, with the most formally acceptable fit (reduced $\chi^2 \sim 10/19 \sim 0.5$) being obtained with an absorbed, single temperature (in equilibrium) plasma model (Raymond & Smith 1977), with line emission from heavy elements similar in abundance to solar values. Table 4 provides results of the model spectra fitted to 3C 434.1.

Confidence level contours of Galactic N_H and temperature were constructed for the fit and are shown in Fig. 7. They indicate little variation in absorption column values with temperature, and a well defined minimum in χ^2 with the value

Table 4. Observed, fitted and calculated properties of the single temperature plasma model with absorption fitted to the PSPC X-ray spectrum (in the range 0.5 keV to 2.4 keV) of 3C 434.1. Solar metal abundance has been assumed. The quality of this fit is $\chi^2/\nu = 14/19$ (ν is the number of degrees of freedom). The PSPC count rate is background-subtracted. The log of the normalization is the volume emission measure over the area of a sphere of radius d, the distance to the source. The fitted value for kT_e indicates a plasma temperature of $T_e = 5.7 \pm 0.4 \times 10^6$ K. A volume filling factor of $f = 0.45$ is estimated from the volume of a shell of thickness to radius ratio 0.15. Uncertainties in kT_e, N_H, and normalization are estimated from a variety of fitted models (with $\Delta\chi^2 \ll 1$) for observed spectra extracted from different areas on the X-ray remnant.

Observed parameters:	
Angular diameter of radio shell	13′
Mean count rate (s^{-1})	0.18 ± 0.01
Distance d (kpc)	4.5 ± 0.5
Diameter (pc)	34 ± 4
Apparent flux F_x (10^{-12} erg s^{-1} cm^{-2})	1.73
Fitted parameters:	
kT_e (keV)	0.38 ± 0.04
log Galactic $N_H(cm^{-2})$	22.20 ± 0.03
Normalization $\log(\int n_e^2 dV/4\pi d^2$ $cm^{-5})$	12.62 ± 0.4
Calculated properties:	
Volume emission measure $\int n_e^2 dV$ (10^{57} cm^{-3})	10.2
RMS electron density n_e (cm^{-3})	0.19
X-ray emitting mass M_x ($M_\odot$)	55
Thermal Eeergy E_{th} (erg)	10^{50}
Unabsorbed flux F_{x0} (10^{-12} erg s^{-1} cm^{-2})	94.2
X-ray luminosity L_x (10^{35} erg s^{-1})	2.3

for Galactic absorption obtained with this model. A column density of Galactic hydrogen $N_H = 1.58 \pm 1 \times 10^{22}$ cm^{-2} is measured. Using the gas to dust ratio of Predehl et al. (1995), $N_H/A_V = 1.79 \pm 0.03 \times 10^{21}$ cm^{-2} mag^{-1}, an optical extinction of $A_V = 8.8 \pm 0.6$ mag is found for the line of sight to the SNR.

The excellent fit of the Raymond-Smith model indicates the X-ray emission is predominantly thermal in origin, and on average the plasma that comprises the X-ray SNR is probably in thermal equilibrium, again indicating that we can treat this SNR as most probably in the adiabatic phase of its evolution.

The most likely origin of the uniform surface-brightness X-ray emission from this SNR is the shock heating of cool H I gas comprising the inside edges of the stellar wind bubble, within which 3C 434.1 is evolving. This process is likely more recent than the epoch of the Hα emission, which probably marks where the shock *first* interacted with the bubble. This appears to be occurring primarily in the Eastern hemisphere, where the bright radio continuum shell correlates very well with X-ray emission (which itself suggests a denser medium than in the west). However, if this is the situation, then the X-ray emitting plasma does not uniformly fill the SNR interior; on the contrary, the plasma will be concentrated at the location of the interaction. The volume fraction of a spherical distribution for the X-ray emission (radius 17 pc) will therefore be much less than unity. One calculates a reasonable volume of interaction by assuming the X-ray emitting mass is from both inside edges of the SWB, concentrated in a shell whose thickness-to-radius ratio is $\Delta R/R = 0.1$–0.15 (that observed for the radio shell). The volume of this shell is thus $V = 4\pi R^2 \Delta R = 0.6\pi R^3$, giving a volume filling factor of $f = V/V_{sphere} = 0.3$–0.45.

The volume-averaged rms thermal electron density $n_e = 0.19\,cm^{-3}$ and the mass of X-ray emitting material $M_x = 55\,M_\odot$ (assuming 35% of the mass is Helium) are calculated using a value for f of 0.45. These properties are markedly different from that found for the Hα, confirming that these emissions originate with different SNR components.

7. Physical conditions and characteristics

Having securely concluded that the emission from 3C 434.1 is indicative of an advanced stage of evolution, some physical characteristics for this SNR are presented using standard shock theory (McKee & Hollenbach 1980) and a Sedov model.

Firstly, our independent distance estimate ($d = 4.5 \pm 0.5$ kpc) allows us to estimate the X-ray luminosity, and hence the mass swept up by the expanding SNR ejecta. If we assume the extreme that all swept-up matter is emitting X-rays one can check that the mass of X-ray emitting plasma from Sect. 6 is consistent with that calculated by the Sedov solution (Kassim et al. 1994):

$$M_{su} = 3.67 \times 10^{-9} P(\Delta E, T)^{-0.5} \theta^{1.5} F_{x0}^{0.5} d^{2.5} (M_\odot) \quad (4)$$

where θ is the diameter of the shell (in arcminutes). This is independent of the explosion energy and ambient density, instead relying on the X-ray plasma temperature. $P(\Delta E, T)$ is the power emitted in the X-ray band (width ΔE) via line radiation by a hot tenuous plasma of Solar abundance. For the ROSAT band (0.5 keV–2.4 keV) and a plasma temperature of $T_e = 4.5 \times 10^6$ K, $P(\Delta E, T) = 1.12 \times 10^{-23}$ erg cm^3 s^{-1} (see Tucker & Koren 1971). One finds $M_{su} \sim 61\,M_\odot$, which is comparable to the $55\,M_\odot$ found emitting X-rays in a shell of radius $R = 17$ pc and thickness ratio $\Delta R/R = 0.15$ ($f = 0.45$). I hereafter will treat the X-ray emission as originating from interaction of the shock with the inside wall of the surrounding H I shell.

An estimate of the SNR shock's expansion velocity v_s can be calculated from the X-ray temperature with:

$$kT_s = 2(\gamma - 1)(\gamma + 1)^{-2} \overline{m} v_s^2 \quad (5)$$

from the conditions for a strong shock (McKee & Hollenbach 1980), where $\overline{m}$ is the mean mass per ion. For the usual specific heat ratio of $\gamma = 5/3$, and some assumptions of the shocked gas' composition (fully ionized, [He]/[H] = 0.1, $\overline{m} \sim 0.62$), a shock velocity $v_s = 560$ km s^{-1} is found to correspond with the X-ray temperature. The equation is accurate to 30% for shocks with Alfvén Mach numbers >6 (a condition certainly found in SNR shock waves).

A lower limit to the initial explosion energy ϵ_0 is obtained by first estimating the thermal energy content of the X-ray emitting mass: $E_{th} = 3/2 M_x/\overline{m} k T_s \simeq 10^{50}$ erg. For a remnant evolving into a uniform medium (with kinetic energy

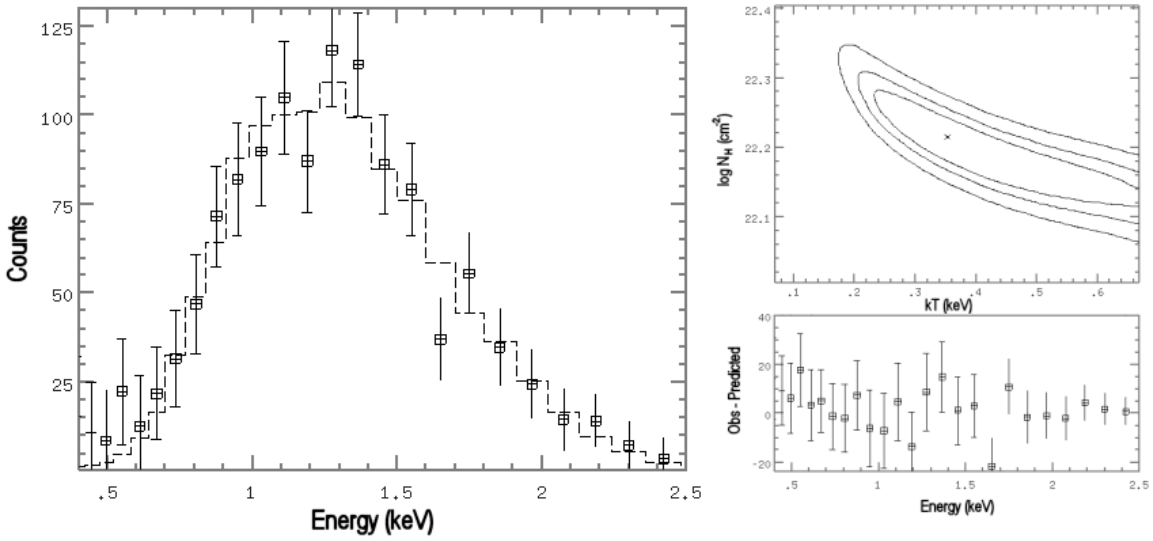

Fig. 7. *Left*: the X-ray spectrum observed by ROSAT (boxes with error bars) and the fitted model spectrum of an absorbed single temperature plasma. The model was fitted to the energy range shown (0.5–2.4 keV), as no significant X-ray emission from the SNR is observed at lower energies. *Right*: the residuals (*top*), and contours of equal χ^2 in the Galactic $N_{\rm H}$-$kT_{\rm e}$ plane for the thermal model spectrum fitted to the ROSAT X-ray data (*bottom*). Levels are at 68% (1σ), 90%, and 99% confidence, and the best fit coordinate (with $\chi^2/\nu \sim 0.5$) is marked with the cross. The absorbing column $N_{\rm H}$ is very nearly constant with varying temperature.

$E_{\rm k} = 1/2 M_{\rm x} v_{\rm s}^2$), Eq. (5) together with $E_{\rm th}$ shows a relationship of:

$$E_{\rm k}/E_{\rm th} = \frac{1}{6}\frac{1}{\gamma - 1}(\gamma + 1)^2 = 1.8. \quad (6)$$

The initial explosion energy of 3C 434.1 shown by the X-ray emission is thus $\epsilon_0 = E_{\rm th} + E_{\rm k} \sim 2.7 \times 10^{50}$ erg. Being in the uncommon position of having an independent distance to the SNR ($d = 4.5 \pm 0.5$ kpc), one can also estimate the total explosion energy ϵ_0 via the Sedov expression (Kassim et al. 1994) and the X-ray flux:

$$\epsilon_0 = 0.115 \times 10^{-6} P(\Delta E, T)^{-0.5} \theta^{1.5} F_{\rm x0}^{0.5} T d^{2.5} (10^{51}\ {\rm erg}) \quad (7)$$

where d is in kiloparsecs. This equation assumes that the SNR X-ray emission with unabsorbed flux $F_{\rm x0}$ and within an angular diameter θ (in arcminutes) provides a reliable record of the shock's position and velocity. If one takes $\theta = 26'$ (the angular diameter of the radio and X-ray SNR), then $\epsilon_0 = 3.4 \times 10^{50}$ erg, comparable to that derived from $E_{\rm th} + E_{\rm k}$, as it should be if the X-ray emission is from an adiabatically behaving shell.

However, the moderately low radio spectral index found over the whole SNR ($\alpha = 0.38$, see Sect. 3.1) suggests that portions of the shock delineated by the radio shell may not be travelling at the velocity suggested by X-ray emission, and that parts of the remnant outside of the X-ray emission are perhaps in a radiative phase. This is the case for the material seen in the Hα line (see Fig. 4), which is observed to be anticorrelated with the X-ray emission. It is likely that this emission originates where the blast wave has driven into the SWB interior wall (density $n_{\rm HI} = 13$ cm^{-3}), and the optical emission traces post-shocked gas that is rapidly cooling and compressed. The mean electron density from the Hα portion ($n_{\rm e} = 40$ cm^{-3}) is three times that of H I in the SWB wall (13 cm^{-3}, Paper II), and somewhat near the limit of $4n_0$ that a nonradiative shock could produce (McKee & Hollenbach 1980). A large uncertainty is attached to this estimate however, as one does not know the thickness of the H II emission region (Sect. 5). For the current estimate of 3 pc, the column density of the H II layer is $N_{\rm tot} \sim 4 \times 10^{20}$ cm^{-2}. A shock is radiative if the column density of swept-up gas exceeds $N_{\rm cool}$, the characteristic density of post-shock gas cooled to $T = 10^4$ K (McKee & Hollenbach 1980):

$$N_{\rm tot} > N_{\rm cool}(T_{\rm s} = 10^4{\rm K}) \simeq 2 \times 10^{17} v_{\rm s7}^{4.2} \left({\rm cm}^{-2}\right) \quad (8)$$

where $v_{\rm s7} \equiv v_{\rm s}/10^7$ cm s^{-1}. If the shock entered the SWB wall with $v_{\rm s} \sim 560$ km s^{-1}, the observed column density of H II indictaes the shock will *just* be radiative, as $N_{\rm cool} = 3 \times 10^{20}$ cm$^{-2} \sim N_{\rm tot}$ in the regions of Hα emission.

Two scenarios are possible to explain the Hα emission from the remnant. The location of the H II could mark where the shock has (in advance of the rest of the shell) penetrated the near (or far) inside of the SWB wall and become radiative. This is quite possible as the SNR is not centered within the SWB, and portions of the blast wave may have arrived at the wall in advance of much of the rest of the SNR. Possibility two is that the shock has just recently begun to interact with the wall (along with the rest of the shell) and has become radiative due to a higher than average density of H I at its location. This scenario is also entirely possible due to the fragmentary or clumpy appearance of the SWB.

Nonetheless, I conclude the following for SNR 3C 434.1. The X-ray emission marks where the shock is just beginning to interact with the SWB wall, and is still adiabatic over most of the shell. The Hα emission is consistent with where the shock has driven into the SWB wall and turned radiative, due to interaction with a clump of much higher density than the rest of the wall and/or because it arrived there some time ago (i.e. the explosion was not centered within the SWB).

7.1. The magnetic field and synchrotron energy in 3C 434.1

In Sect. 3.1, the power-law spectrum $S_\nu \propto \nu^{-0.4}$ describes the observed radio spectrum of 3C 434.1 over a wide range of frequencies ($\nu_{\rm min}$ = 151 MHz to $\nu_{\rm max}$ = 4.75 GHz). Let us make use of this well-determined measure and examine the magnetic and energetic properties of the synchrotron-emitting region of this SNR.

If a randomized magnetic field pervades the synchrotron-emitting region, then one can determine the field strength and total energy of the relativistic electrons by assuming equal partitioning of the energy-density stored in the field and characterizing the relativistic electrons:

$$\int_{E_{\rm min}}^{E_{\rm max}} N(E) E {\rm d}E = \frac{B^2}{2\mu_0} \tag{9}$$

where $N(E)$ is the number of electrons per unit volume in the energy interval E to E + dE, and electron energies are determined by the observed frequency range with $E_{\rm min,max} = 2.5\times10^{-4}\,(\nu_{\rm min,max}/y_{1,2}(p)B)^{1/2}$ MeV, with the functions $y_{1,2}(p)$ as tabulated in Ginzburg & Syrovatskii (1965). A power-law distribution well defines the observed spectrum (see Fig. 2), and so the electron energy distribution can be similarly described by $N(E) = \kappa E^{-p}$, where energy index p is related to spectral index α by $\alpha = (p-1)/2$.

For a randomly oriented field, the synchrotron radiation spectrum for this energy distribution is (Longair 1994, Eq. (18.49)):

$$J(\nu) = \frac{\sqrt{3}e^3 B\kappa}{4\pi\epsilon_0 m_{\rm e} c}\left(\frac{3eB}{2\pi\nu m_{\rm e}^3 c^4}\right)^{(p-1)/2} \times \frac{\sqrt{\pi}}{2}\frac{\Gamma(\frac{p}{4}+\frac{19}{12})\Gamma(\frac{p}{4}-\frac{1}{12})\Gamma(\frac{p}{4}+\frac{5}{4})}{(p+1)\Gamma(\frac{p}{4}+\frac{7}{4})} \tag{10}$$

where $J(\nu) = 4\pi I_\nu/s$, and s is the path length through the synchrotron-emitting region (the synchrotron emission is assumed optically-thin). Completing the integral in Eq. (9), and combining with Eq. (10) gives us the following set of non-linear equations:

$$\begin{aligned} \kappa &= c_1 B^2 \\ \kappa B^{(p+1)/2} &= c_2 \end{aligned} \tag{11}$$

where c_1 and c_2 are constants that depend on $E_{\rm min,max}$ and $J(\nu)$ respectively. Our method of calculation begins with a trial magnetic field $B_{\rm trial}$, from which one finds $E_{\rm min,max}$. With the observed spectrum parameters $\nu_{\rm min,max}$, S_ν and α making up constants c_1 and c_2, the field strength B and energy distribution coefficient κ are readily determined by the solution of Eq. (11). The process is then iterated with B taking the place of $B_{\rm trial}$ in $E_{\rm min,max}$. This method settles to a solution after only a few iterations, even if one starts with an extreme low or high initial value for $B_{\rm trial}$.

The thickness-to-radius ratio of the shell in 3C 434.1 is estimated from the 21 cm radio continuum image to be ~0.15 (see Sect. 5). To explain the X-ray and Hα emission so prominent of the eastern half of the SNR, it is suggested that 3C 434.1 is displaced from the centre of bubble east and along the line of sight, being closer to the eastern and front stellar wind bubble wall. In this situation, the filled-centre synchrotron emission arises from the interaction of the SNR shock with the inner-edges of the H I bubble's wall.

Table 5. The magnetic and energetic properties of the synchrotron environment in SNR 3C 434.1, calculated by assuming the particle and field energies are close to equipartition.

Input parameter	Value
Initial field $B_{\rm trial}$	2 μG
Electron energy spectrum index p	1.76
LOS dimension of emitting region s	5.3 pc
Volume of emitting region V	2.8×10^{59} cm^{-3}
Solution	**Value**
Magnetic field stength B	16 μG
Lower energy $E_{\rm min}$	0.27 GeV
Upper energy $E_{\rm max}$	54 GeV
Energy spectrum coefficient κ	2.7×10^{-11}
Electron density $n_{\rm synch}$	2.8×10^{-9} cm^{-3}
Total energy of synchrotron emission $W_{\rm tot}$	5.8×10^{48} erg

Table 5 presents the solution, based on the line-of-sight dimension of the radio emitting region (s) estimated by assuming the synchrotron emission is concentrated in the spherical SNR shell and the total path through the interacting zone is $s \sim 5$ pc. To account for electron energies beyond our observed frequency range, I extend our upper limit to $\nu_{\rm max}$ = 20 GHz (for which the flux density is calculable from the power law of Sect. 3.1). A field strength of B = 15 μG is found for electrons in the energy range 0.6–56 GeV. As an estimate of the magnetic field just behind the shock front, this is consistent with a factor of 3–4 enhancement of the mean ISM field of $B_{\rm tot} \sim 4$–$5\,\mu$G (estimated from the model of Strong et al. 2000). If the synchrotron emission is distributed uniformly throughout the shell's volume, then one finds $B \sim 7\,\mu$G, much less consistent with the above Galactic field. The *minimum* magnetic field that accounts for the observed flux at 1420 MHz (the condition for which is equipartition of field and particle energies) in the radio shell is:

$$B_{\rm min} = 1.8\left(S_\nu 4\pi d^2/V\right)^{2/7}\nu^{1/7} = 10\,\mu{\rm G} \tag{12}$$

where S_ν, distance d and volume V are in SI units (Longair 1994). As this is higher than the field calculated for a uniformly filled sphere, this suggests the relativistic electrons occupy a fraction of the total SNR volume, the same situation for the X-ray emission.

The total energy contained in both the relativistic electron plasma and the magnetic field from this method is $W_{\rm tot} \sim VB^2/\mu_0 = 5\times10^{48}$ erg, where the volume of the half-shell

(as in Sect. 6) is $V = 4\pi R^2 \Delta R \sim 3 \times 10^{59}$ cm^3. It is evident that the energy of the radio emission is small compared to the explosion energy of the SNR (calculated in Sect. 7). A tenuous relativistic plasma (density $n_{\rm synch} = 1.4 \times 10^{-9}$ cm^{-3}) is the source of radio emission from 3C 434.1.

The energy of the radio emission is similar to the thermal energy found in the optical component of the remnant's emission spectrum. An integrated radio luminosity of $L_{\rm radio} = 4.4 \times 10^{34}$ erg s^{-1} is found (for the frequency range 151 MHz to 20 GHz), two orders of magnitude lower than the optical luminosity, and one order lower than the X-ray. The results of these analyses show that losses from synchrotron are insignificant when compared to the thermal energy radiated away by the X-ray emitting plasma and the ionized hydrogen.

8. Discussion

We have here a unique system, that exhibits characteristics of three SNR evolutionary phases. 3C 434.1 was formed inside a pre-existing stellar-wind bubble of interior density ~0.1 cm^{-1}. At the time of its demise, the progenitor was located off-centre with respect to the SWB centre, nearer to the eastern edge of the SWB wall. The remnant's shock front initially advanced a considerable distance into this environment without collecting much material, essentially staying in the free-expansion phase (Fabian et al. 1983, show that SNRs evolving into stellar wind-blown regions continue to expand freely out to large radii). The western half of the SNR is likely still freely expanding west into the central interior of the bubble, and is dimly visible in radio continuum (and invisible in optical and in X-ray lines) as it has not encountered much intra-bubble matter.

The first area of the shock front's interaction with dense H I comprising the bubble wall is found where the optical emission is visible (the far eastern SWB face). The blast wave ($v_{\rm s}$ = 560 km s^{-1}) was driven into the inside wall ($n_{\rm b} \sim 13$ cm^{-3}) compressing the material to ~$3n_{\rm b}$ (40 cm^{-3} is measured from the optical emission), and the resulting substantial Lyman-α radiation ionizing it. Assuming pressure equilibrium, the shock velocity in the bubble wall ($v_{\rm b}$) would be reduced by the factor $v_{\rm b}/v_{\rm s} = (\beta n_0/n_{\rm b})^{1/2} = 0.0031$, where the bubble interior density (for a "typical" H I SWB, Weaver et al. 1977, Fig. 3 of that paper) is $n_0 \sim 0.02$–0.04 cm^{-3} and β is a dimensionless parameter of order ~4.4 (for a density contrast of 1:100, Lozinskaya 1992). Considerable energy would be radiated away downstream of the shock by cooling, and the shock turned radiative. Optical recombination emission is expected from these ionized zones in front of and behind radiative shocks. The correlation of optical emission with strong non-thermal radio emission shows the presence of the shock in the area.

The X-ray emission from 3C 434.1 demarcates an interaction zone with the SWB wall that is somewhat younger than the region of optical emission. The general correlation of X-ray with the synchrotron shell shows the location of the shock here. It is likely that the interacting zone is at both the front and back inside-edge of the shell. Radiative cooling here has not yet become dominant, and this is an adiabatically evolving portion of the SNR. As one does not see substantial emission from the westerly extension of the remnant (near the bubble's centre), this eastern shock front (closer to the wall) must have accumulated more intrabubble matter. Since the electron density ($n_{\rm e} \sim 0.2$ cm^{-3}) for the X-ray region is so different from the optical emission, it is likely that the shock here has not yet been fully driven into the shell (as it has in the optical-emitting layer). The expanding SNR has nevertheless accumulated enough material (55 $M_\odot$) to slow down. Weaver et al. (1977) show that a sharp rise in density (up to $2\rho_0$ at $0.98R$) occurs approaching a typical stellar wind bubble's inside edge. The layer of X-ray emission is probably nearing the inner edge, and the shock front (upstream) has just entered the SWB wall. Here, the SNR would have accumulated much of its swept-up material quite recently.

8.1. An interaction model of SNR 3C 434.1

I present here an original approach to obtaining a solution for the SN event that produced 3C 434.1, alternative to the standard Sedov model. This simple idea makes use of theory for the interaction of SN with circumstellar bubbles (e.g. Chevalier & Liang 1989), and constrains it with our observations such that a unique solution for 3C 434.1 is possible.

With the conditions that a) 3C 434.1 is just beginning to encounter the stellar-wind H I shell, and b) the western extension of the remnant is still freely expanding, one can solve for the initial conditions and age of the explosion. The equation for the time to the initial shell (radius R) interaction is (Chevalier & Liang 1989):

$$t_{\rm i} = \left[\frac{nM_1}{(n-3)\alpha M_{\rm ej}}\right]^{1/(n-3)} R \left[\frac{10(n-5)\epsilon_0}{3(n-3)M_{\rm ej}}\right]^{-1/2} \quad (13)$$

where n is the index of a power-law describing the density profile in the outer part of the initial supernova explosion, $M_{\rm ej}$ is the mass of ejecta in the SN, and M_1 is the mass lost to the bubble interior by the stellar winds. The value of α (obtainable from Chevalier 1982) is 4.9 for $n = 6$, and 1.5 for $n = 9$ ($n = 5$ is the standard Sedov solution). From Paper II, we know much about the bubble surrounding 3C 434.1 and its stellar residents (three B0V and one O4V type stars), and have estimated the SNR progenitor type to be O4V.

The total mass donated to the bubble interior over the MS lifetime of these stars ranges from $M_1 \sim 12$–$26\ M_\odot$ (depending on mass-loss rates assigned to the O4 stars; e.g. Howarth & Prinja 1989; and Chevalier & Liang 1989). However, it is likely that mass lost during the main sequence is part of the SWB shell already, and that the mass inside the SWB comes mainly from the SNR projenitor's prodigous output as a Wolf-Rayet star. For $\dot{M} \sim 5$–$6 \times 10^{-5}\ M_\odot$ yr^{-1} (Langer 1989) an intrabubble mass of M_1 ~25 $M_\odot$ here is estimated (assuming a He burning phase lifetime of $\sim 5 \times 10^5$ yr).

Now, let us require that $\epsilon_0 = 1/2 M_{\rm ej} v_{\rm s0}^2$ (where $v_{\rm s0}$ is the initial blast-wave velocity). Here ϵ_0 is the lower limit (2.7×10^{50} erg) found from shock theory (Sect. 7). Further, let us also assign the expansion velocity of the western hemisphere of 3C 434.1 (for which the current radius is $R_{\rm west} \sim 29$ pc) to be $v_{\rm s0} \sim R_{\rm west}/t_{\rm i}$. These two conditions together with Eq. (13) form a set of non-linear equations for unknowns $t_{\rm i}$, $M_{\rm ej}$, and $v_{\rm s0}$.

Table 6. The input parameters and solution to the model of Chevalier & Liang (1989), describing the interaction of 3C 434.1 with the inner wall of its parent stellar wind bubble.

Parameter	Value
Observable:	
Radius of SWB R (pc	30
Radius of western SNR $R_{\rm west}$.	29
Intrabubble mass (from SNR projenitor) M_1 ($M_\odot$)	25
Explosion energy ϵ_0 (erg)	2.8×10^{50}
Shock velocity $v_{\rm s}$ (km s^{-1})	560
Model:	
Order of SN outer density profile n	6
Total mass in explosion $M_{\rm ej}$ ($M_\odot$)	15.5
Time to interaction $t_{\rm i}$ (yr)	25 300
Shock velocity in W expansion $v_{\rm s0}$ (km s^{-1})	1350
Shock velocity in E interaction $v_{\rm i}$ (km s^{-1})	580

An iterative numerical computation is used to explore solutions for a range of indices $n = 6$–9.

To determine which solutions best describe 3C 434.1, the solution must be checked against two observable conditions. Firstly, the ejecta mass must be greater than the mass of hot shocked intrabubble gas when the interaction region reaches the edge of the bubble, or $3M_{\rm ej}/n > \zeta M_1$ (Chevalier & Liang 1989, where ζ is 0.93 for $n = 9$ and 0.28 for $n = 6$, tabulated in Chevalier 1982). Secondly, the shock velocity just before the interaction $v_{\rm i} = (n-3)/n \times R/t_{\rm i}$ should be comparable to that calculated from shock theory (560 km s^{-1}).

Appropriately satisfying both conditions is the solution for $n \simeq 6$ (tabulated in Table 6). The initial mass in the explosion is $M_{\rm ej} \sim 15\ M_\odot$, and the likely interaction time is $t_{\rm i} \sim 25\,000$ yr. The mean free-expansion velocity of the western hemisphere of 3C 434.1 is $v_{\rm s0} \sim R_{\rm west}/t_{\rm i} = 1350$ km s^{-1}. This velocity and ejecta mass are consistent with a type Ib SNe (Lozinskaya 1992), the type deduced in Paper II. The shock velocity just prior to the interaction with the shell is $v_{\rm i} = (n-3)/n \times R/t_{\rm i} \sim 580$ km s^{-1}, consistent with shock theory. These are likely rough estimates for $M_{\rm ej}$, n, $t_{\rm i}$ and $v_{\rm s0}$, as one does not know M_1 or ϵ_0 well (among other values). Nevertheless, models of SNR interaction with SWBs are more realistic than the standard Sedov model for 3C 434.1.

Acknowledgements. The Dominion Radio Astrophysical Observatory is operated as a national facility by the National Research Council of Canada. I thank Roland Kothes and Tom Landecker of DRAO for their participation in helpful and engaging discussions. Dan Harris and Amy Mossman of CfA (Harvard) graciously assisted with X-ray analysis software issues. E. Pfeffermann was the original P.I. for the ROSAT observations I have used within. I thank the referee, who has provided very helpful comments and suggestions which have clarified this manuscript. This work was supported by a Natural Sciences and Engineering Research Council (NSERC) Graduate Scholarship to TF.

References

Acker, A., Koppen, J., Stenholm, B., & Jasniewicz, G. 1989, A&AS, 80, 201
Chevalier, R. A., & Liang, E. P. 1989, ApJ, 344, 332
Chevalier, R. A. 1982, ApJ, 258, 790
Dame, T. M., Hartmann, D., & Thaddeus, P. 2001, ApJ, 547, 792
Fabian, A. C., Brinkman, W., & Stewart, G. C. 1983, in Supernova Remnants and Their X-ray Emission, ed. J. Danziger, & P. Gorenstein (Dordrecht: Reidel), IAU Symp., 101, 119
Fesen, R. A., Winkler, F., Rathore, Y, Downes, R. A., & Wallace, D. 1997, AJ, 113, 767
Fesen, R. A., & Hurford, A. P. 1996, ApJS, 106, 563
Fesen, R. A., & Hurford, A. P. 1995, AJ, 110, 747
Foster, T. 2005, ApJ, submitted
Foster, T., & Routledge, D. 2001, A&A, 367, 635 (Paper I)
Foster, T., & Routledge, D. 2003, ApJ, 598, 1005
Foster, T., Hube, D., Couch, J., et al. 1999, in Precision CCD Photometry, ed. E. R. Phillips, D. L. Crawford, & R. A. Tucker (San Francisco: ASP), ASP Conf. Ser., 189, 111
Foster, T., Routledge, D., & Kothes, R. 2004, A&A, 417, 79 (Paper II)
Fürst, E., Reich, W., Reich, P., & Reif, K. 1990, A&AS, 85, 691
Ginzburg, V. L., & Syrovatskii, S. I. 1965, ARA&A, 3, 297
Goss, W., Mantovani, F., Salter, C. J., Tomasi, P., & Velusamy, T. 1984, A&A, 138, 469
Haslam, C. G. T., Salter, C. J., Stoffel, H., & Wilson, W. E. 1982, A&AS, 47, 1
Howarth, I. D., & Prinja, R. K. 1989, ApJS, 69, 527
Kassim, N. E., Hertz, P., Schuyler, D., Van Dyk, & Weiler, K. 1994, ApJ, 427, L95
Keyes, C. D., Aller, L. H., & Feibelman, W. A. 1990, PASP, 102, 59
Landecker, T. L., Higgs, L. A., & Roger, R. S. 1985, AJ, 90, 1082
Landecker, T. L., Dewdney, P. E., Burgess, T. A., et al. 2000, A&AS, 145, 509
Langer, N. 1989, A&A, 220, 135
Longair, M. S. 1994, High Energy Astrophysics (New York: Cambridge University Press), 2,
Lozinskaya, T. 1992, Supernova and Stellar Wind in the Interstellar Medium (New York: American Institue of Physics)
Manchado, A., & Pottasch, S. R. 1989, A&A, 222, 219
Mantovani, F., Nanni, M., Salter, C., & Tomasi, P. 1982, A&A, 105, 176
McKee, C., & Hollenbach, D. J. 1980, ARA&A, 18, 219
Predehl, P., & Schmitt, J. H. M. M. 1995, A&A, 293, 889
Raymond, J. C., & Smith, B. W. 1977, ApJS, 35, 419
Reich, W., Reich, P., & Fürst, E. 1990, A&AS, 83, 539
Rengelink, R. B., Tang, Y., de Bruyn, A. G., et al. 1997, A&AS, 124, 259
Rohlfs, K., & Wilson, T. L. 1996, Tools of Radio Astronomy, 2nd edition (Berlin: Springer-Verlag)
Seward, F. D., & Velusamy, T. 1995, ApJ, 439, 715
Stetson, P. B. 1987, PASP, 99, 191
Strong, A. W., Moskalenko, I. V, & Reimer, O. 2000, ApJ, 537, 763
Taylor, A. R., Gibson, S. J., Peracaula, M., et al. 2003, AJ, 125, 3145
Tucker, W. H, & Koren, M. 1971, ApJ, 168, 283; erratum, ApJ, 170, 621
Vessey, S. J., & Green, D. A. 1998, MNRAS, 294, 607
Weaver, R., McCray, R., Castor, J., Shapiro, P., & Moore, R. 1977, ApJ, 218, 377
Young, J. S., & Scoville, N. Z. 1991, ARA&A, 29, 581